Christian Winter, Ingo Scholz, Stephan Rupp, Thomas Wittenberg

Reconstruction of tubes from monocular fiberscopic images – Application and first results

appeared in:
Vision, Modeling, and Visualization 2005
Erlangen, Germany
pp. 57–64

Reconstruction of tubes from monocular fiberscopic images – Application and first results

Christian Winter[1,3], Ingo Scholz[2], Stephan Rupp[1], Thomas Wittenberg[1]

(1) Fraunhofer Institute of Integrated Circuits IIS,
Am Wolfsmantel 33, 91085 Erlangen, Germany
(2) Chair of Pattern Recognition, University Erlangen-Nuremberg,
Martensstr 3, 91058 Erlangen, Germany
(3) Chair of Information Technologies,
University Erlangen, Am Wolfsmantel 33, 91058 Erlangen, Germany
Email: {wnt,ruppsn,wbg}@iis.fraunhofer.de
Email: ingo.scholz@informatik.uni-erlangen.de

Abstract

In many industrial and medical applications, glass-fiber endoscopes are used to acquire images from complex hollows for diagnostic and interventional purposes. For a complete exploration and understanding of a hollow cave, 3-d reconstruction is necessary. In contrast to other endoscopy-based reconstruction scenarios, in our case the images are immensely degraded by the glass-fiber honeycomb-pattern. Thus, we propose a reconstruction scheme for fiberscopical obtained image sequences, which has been enhanced by a data driven preprocessing step as well as a knowledge driven post-processing step. By example of a 3-d reconstruction of a straight circular tube from monocular fiberscopic images, these extensions are analyzed and evaluated.

1 Introduction and Objective

Many applications in the domain of industrial and medical image processing make considerable use of flexible endoscopes - so called 'fiberscopes' or 'boroscopes' - to gain visual access to holes, hollows, antrums and cavities that are difficult to enter and examine. Common to both application fields are usually very small natural or man-made entry points to the observed scene - with diameters below 4 mm - as well as the complexity of the hollow itself, forbidding the use of rigid lens-based endoscopes. Typical examples in the field of industrial machine inspection are complex drill holes or coolant bores in turbine blades [11, 8, 1, 12].

In the medical domain, fiberscopes are applied for diagnostic tasks, such as laryngoscopy [29, 2], bronchoscopy [5, 20], as well as for minimal-invasive surgery-scenarios [16, 30, 15].

1.1 Introduction to Fiberscopes

Due to the nature of light transmission into the observed cavity and image transmission out of the cavity by the sole use of glass fibers, the acquired and observed image scene is sub-sampled by the amount of glass fibers that form the flexible image conductor. The amount of fibers depends on the diameter of the endoscope and the physical dimensions of the fibers. Typical numbers of glass fibers for image transmission in such flexible endoscopes are in the range between 3,000 and 50, 000 fibers, where each of the glass fibers carries only one intensity information. In comparison, the spatial resolution of cameras begin at the low end with 307,200 pixels, commonly used by web-cams, or television cameras with a resolution of approximately 512×728 pixels. At the high end, modern cameras for application in industrial and medical fields are available starting at one mega-pixel and currently range up to 12 mega-pixels. Thus, using fiberscopes in combination with cameras and the goal to observe, acquire, digitize and reconstruct a complex scene of a cavity, a crude sub-sampling is made on the tip of the fiberscope, while an over-sampling takes place, where the image transmitted by the glass fibers is acquired with a camera. An image of a test-chart, observed with a fiberscope is depicted in Fig. 1, with sub-regions enlarged to show the typical fiber-effect. It can be seen, that each group of pixels - denoting the intensity of an image point transmitted by a glass fiber

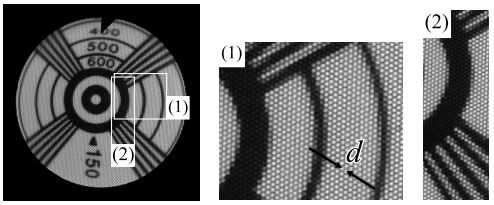

Figure 1: *Typical view through a fiberscope (left) onto a test chart. Enlarged sections (center and right) depict the homogeneous honeycomb structure from the glass fiber transmission*

- is surrounded by a dark ring. This is due to the transmission property of glass fibers. Every optical fiber consists of a core with a high refractive index n_1 and a cladding with a lower refractive index n_2. Light rays, which enter the fiber at one end, are guided along the core by total internal reflections at the core-cladding interface. This total internal reflection can be described by Snellius' law: $\sin \alpha_T = n_2/n_1$, where α_T denotes the critical angle of total reflection. The reflected light rays follow the bends in the fiber and exit it at its other end. For fiberscopes, bundles of optical fibers are combined with appropriate end terminations and protective sheathing to form light guides.

The elastic image conductor of current available fiberscopes consists of a sorted bundle of fibers made of glass or quartz crystal. According to the desribed core-cladding relationship, fibers show a homogeneous alignment of bright transmission points, surrounded by a dark borders over the entire image, the so-called 'comb' structure (see Fig. 1, center and right).

1.2 Objective

Within the scope of our project, the future goal is the reconstruction of complex hollow spaces from monocular fiberscopic views . In contrast to other work, where rigid rod-lens endoscopes for scene exploration are applied [22, 26, 10], the reconstruction process in our work is strongly dependend on the prepocessing steps to eliminate the honeycomb artifacts, as depitected in Fig. 1.

Thus, in this context the objective of the presented work is

- to propose the established method of Heigl [6] for camera pose estimation and 3-D scene reconstuction, which has been extended by
- a data driven spectral filtering prepocessing step to eliminate the honeycomb structures, and
- a knowledge driven extension of the reconstruction to eliminate false point positions. Finally,
- the achieved preliminary reconstruction results will be presented and subjectively evaluated with respect to the honey-comb removing filtering approach at the beginning of the processing chain and the elimination of bad tracking points in the progress of reconstruction.

The remainder of this article is organized as follows: After briefly reviewing work from literature about endoscopy-based scene reconstruction (section 2), we will propose our enhanced reconstruction scheme (section 3) including the steps image filtering, calibration and distortion, tracking, self-calibration and reconstruction as well as some knowledge-driven extensions. Section 4 resumes the proposed approaches and presents results for different experimental settings. We end this work with a discussion and conclusion of the obtained results in section 5.

2 State of the art

To our knowledge there are not many publications with respect to 3-D reconstruction of tubes or complex hollows based on monocular fiberscopical acquired images. Even though literature has addressed several 3-D-reconstruction schemes based on image sequences obtained with rigid endoscopes or video-endoscopes for various applications, no work about scene reconstruction from fiberscopic images is known.

Vogt et al [26, 25] introduced a reconstruction and lighfield-visualisation of the abdomen, based on a roboter-mounted rigid endoscope. Similar work has been known from Thormäehlen et al [22, 21], based on image sequences obtained from a video-endoscope in the colon. The scene reconstruction is done in two steps, first the movement of the videoscope itsself is approximated, and secondly a 3-d reconstruction is calulated. A reconstruction scheme for tubes – similar to our appraoch – has been suggested by Kübler et al [10], which is also based on video-endoscopic images and uses an external localisation system for affine motion information. The 3-d-reconstruction itsself is based on a piece-wise ring-model of the tube.

The closest work to our own investigations has been proposed by Müller et al [13, 14], who use a

fiberscope to measure the stenosis of the trachea, based on an active illumination approach. For this method, a cone mirror is used to project a ring-shaped laser beam to the inner walls of the trachea and thus illuminating the tracheal wall in a piece-wise manner for measurement and reconstruction.

3 Method

Our proposed method consists of four major steps. The first step (section 3.1) consists of an adaptive filtering approach, making the feature and correspondence detection more robust. The second step deals with the calibration and distortion correction, which will be discussed in section 3.2. The third step consists of the correspondence-calculation and feature-tracking (section 3.3). This part also includes the 3-D-reconstruction process as well as self-calibration. Finally, in section 3.4, the forth step is outlined, dealing with two knowledge-driven extensions of the reconstruction process, that enhance the results significantly. While the calibration and reconstruction steps (2. and 3.) are based on known methods, they are not applictable in this context without data-driven image filtering (step 1) and knowledge driven exception handling (step 4).

3.1 Filtering

To eliminate the honey-comb stuctures in fiberscopic images (Fig. 2 left), which disturb the feature-extraction process for the 3-D reconstruction, a spectral filtering approach is applied. Based on the spectrum of a fiberscopic image, the Nyquist-Shannon Sampling Theorem is applied to obtain parameters for an optimal band-rejection mask generation. This approach runs in a fully automatic mode and is independent to scale and resolution of the image conductor, as well as type and resolution of the image sensor. Several types of band-rejection masks can be generated by this process, including simple rotation invariant masks as well as star-shaped rotation variant masks, which contain information about orientation between fiberscope and sensor. This filtering approach enables a – subjectively – complete elimination of the fiberscopic comb structure for and is adaptive to any arbitrary endoscope and sensor combinations [27]. Fig. 2 right shows the filtering result from Fig. 2 left.

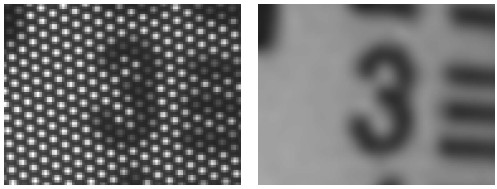

Figure 2: *Left: Original image with honey-comb distortions, acquired with a glass-fiber endoscope, right: filtered and enhanced image*

3.2 Calibration and Distortion Correction

Optical imaging systems utilizing lenses exhibit geometric distortions in the acquired images due to liabilities in lens manufacturing. Especially, when considering wide-angle lenses – as can be found in endoscopes – usually a strong barrel distortion is observable, which necessitates a correction, since quantitative information is derived from the acquired images. These distortions have to be taken into account during the camera calibration process to minimize the model fit error and improve calibration accuracy.

The internal camera geometry and optical characteristics of the imaging system are determined by a well-known calibration technique by Zhang [32], modelling the imaging process by a pinhole camera, and incorporating the perspective projection of 3-D world coordinates onto the 2-D imaging plane. According to this model the mapping of a scene point $\mathbf{X} = (X, Y, Z)^T$ to its ideal 2-D image in sensor coordinates $\mathbf{u} = (u, v)^T$ is given by

$$\lambda \tilde{\mathbf{u}} = \mathbf{A} \begin{pmatrix} \mathbf{R} & \mathbf{t} \end{pmatrix} \tilde{\mathbf{X}} \tag{1}$$

where $\tilde{\mathbf{u}}$ denotes the augmented vector by adding 1 as the last element and $\tilde{\mathbf{X}}$ respectively. λ represents a scalar factor that is due to the homogenous coordinate notation.

The 3×3 rotation matrix $\mathbf{R}$ and the 3×1 translation vector $\mathbf{t}$ express the position and orientation of the camera with respect to the origin of the (user-defined) world coordinate system, and are generally referred to as the *extrinsic parameters*.

In contrast to the pose of the camera, the *intrinsic parameters* refer to the components of the 3×3 *camera matrix* $\mathbf{A}$ describing the image formation

process:

$$\mathbf{A} = \begin{pmatrix} \alpha f & \gamma & u_0 \\ 0 & f & v_0 \\ 0 & 0 & 1 \end{pmatrix} . \quad (2)$$

Its four degrees of freedom are given by the *focal length* f and the *principal point* $\mathbf{u_0} = (u_0, u_0)^T$ of the camera, the *aspect ratio* α of a pixel and the *angle of skew* γ between the two axes of the CCD sensor array, which is frequently set to zero, justified by the virtually orthogonal image axes in most modern CCD cameras.

3.2.1 Camera Lense Distortion

In real optical systems, including endoscopes [19], [24], [31], [3], the idealized pinhole model is often not sufficient to describe the mapping from camera to image coordinates precisely, due to imperfections of the lens(es). These liabilities in lens manufacture are typically modelled by *radial* and *tangential* distortion, which is usually described by four coefficients [7], [9]: two radial distortion coefficients κ_1, κ_2, and two tangential ones ρ_1, ρ_2.

Let (u, v) be true pixel image coordinates, that is, coordinates with ideal projection, and $(\hat{u}, \hat{v})$ be corresponding real observed (distorted) image coordinates. Taking into account two expansion terms gives the following:

$$\begin{aligned} \hat{u} &= u + u(\kappa_1 r^2 + \kappa_2 r^4) \\ &\quad + (2\rho_1 uv + \rho_2(r^2 + 2u)) \\ \hat{v} &= v + v(\kappa_1 r^2 + \kappa_2 r^4) \\ &\quad + (2\rho_2 uv + \rho_1(r^2 + 2v)) \end{aligned}$$

where $r^2 = x^2 + y^2$. The second terms in the above relations describe radial distortion and the third ones tangential distortion. The center of the radial distortion is the same as the principal point. Because $\hat{u} = u_0 + \alpha f u$ and $\hat{v} = v_0 + f v$, where u_0, y_0, α and f are components of the camera intrinsic matrix $\mathbf{A}$, the resulting system can be rewritten as follows:

$$\begin{aligned} \hat{u} = u + (u - u_0)[\kappa_1 r^2 + \kappa_2 r^4 \\ + 2\rho_1 y + \rho_2 x(r^2 + 2x^2)] \quad (3) \\ \hat{v} = v + (v - v_0)[\kappa_1 r^2 + \kappa_2 r^4 \\ + 2\rho_2 x + \rho_1 y(r^2 + 2y^2)] . \quad (4) \end{aligned}$$

These parameters extend the set of camera parameters and are reasonably assigned to the intrinsic camera parameters, because they affect the image formation.

The calibration procedure described in [32] calculates both the extrinsic and intrinsic parameters of the imaging system - however only the latter are required for distortion correction as can be seen in equation (3) and (4).

3.3 Tracking, Self-Calibration and Reconstruction

Once an undistorted image stream is available, camera pose estimation and 3-D reconstruction using standard approaches can be attempted. The procedure employed here uses point features based structure-from-motion. Thus, the first step is to detect point features in the first image of the image sequence and to track them through the sequence, replacing lost features in each image. The detection and tracking algorithm is based on the well-known Shi-Tomasi-Kanade tracker [23, 18]. Additionally, the tracker contains a number of extensions such as illumination compensation, outlier detection and "feature drift prevention" for long image sequences, which are explained in detail in [33].

Given a set of features $\mathbf{u}_{i,j}$ which are visible in all images $\mathbf{f}_i$ of a sequence, the camera's extrinsic parameters, i. e., its pose given by the rotation $\mathbf{R}_i$ and translation $\mathbf{t}_i$ of equation (1), and the 3-D positions $\mathbf{X}_j$ of the features can be calculated using a factorization method. In this case the paraperspective factorization by Poelman and Kanade [17] is used.

The result is refined using a non-linear optimization of the back-projection error as proposed in [4]. Since the internal parameters of the camera are known from the previous step, they need not to be estimated here. Thus, the affine reconstruction obtained by the factorization method can be upgraded to an euclidean one by constructing a projection matrix $\mathbf{P}_i$ from $\mathbf{A}$, $\mathbf{R}_i$, and $\mathbf{t}_i$, i. e.,

$$\mathbf{P}_i = \mathbf{A}(\mathbf{R}_i | \mathbf{t}_i) \quad , \quad (5)$$

and minimizing the back-projection error by adjusting $\mathbf{R}_i$, $\mathbf{t}_i$, and $\mathbf{X}_j$. For an estimated projection $\tilde{\hat{\mathbf{u}}}_{i,j} = \hat{\mathbf{P}}_i \tilde{\hat{\mathbf{X}}}_j$ the error is calculated as the difference to the corresponding true image feature $\mathbf{u}_{i,j}$,

$$\boldsymbol{\epsilon}_{i,j} = \mathbf{u}_{i,j} - \hat{\mathbf{u}}_{i,j} \quad . \quad (6)$$

$\hat{\mathbf{u}}_{i,j}$ denotes the estimated image feature $\tilde{\hat{\mathbf{u}}}_{i,j}$ in cartesian coordinates. The total back-projection error for image $\mathbf{f}_i$ is thus defined as $\boldsymbol{\epsilon}_i^T \boldsymbol{\epsilon}_i$, $\boldsymbol{\epsilon}_i$ being the

concatenation of all $\epsilon_{i,j}$ in a single column vector. The camera parameters are optimized for each image seperately, and each iteration is alternated with an iteration of the 3-D point position optimization. The Levenberg-Marquardt extension of the Gauß-Newton algorithm is used for optimization.

Especially for the low-quality endoscopic images used here, the condition that the features are visible in all images is only valid for few images at a time. Therefore, this initial reconstruction is only applied to a short subsequence, and the reconstruction of the remaining images is added using the iterative procedure described in [6]. The camera parameters for an image neighbouring the already processed image subsequence are estimated again by non-linearly minimizing the back-projection error of the already known 3-D features. The parameters of this camera $\mathbf{P}_k$ are initialized using the parameters of an adjacent, known camera pose $\mathbf{P}_{k\pm1}$. After the estimation of each camera pose, newly appearing features are triangulated in order to compensate for features which move out of the field of vision of the camera. 3-D points with a back-projection error above a certain threshold are discarded. Thus, the reconstruction is extended image by image to the whole image sequence. Since only six parameters have to be estimated for each camera pose (three for the rotation and three for the translation), this process is quite robust and yields good results even for very noisy input data such as in the case at hand.

3.4 Knowledge-driven Extensions

To test the proposed method for 3-D-reconstruction based on monocular, fiberscopic images, reference objects with known shape and geometry have been used for analysis, such as straight, cylindric bore holes. Fig. 3 shows a sequence of images taken at several steps inside the bore. The endoscope has a straight view along the moving axis. In Fig. 4 detected and tracked points (as described in section 3.3) are marked by colored dots.

Due to the image acquisition process with glassfiber-endoscopes, the images are degraded and thus falsly tracked features in some of the so-called trails lead to misplaced 3-d positions. To eliminate such falsly calculated 3-d-point corresponcences from the reconstruction process, we apply knowledge driven extensions. From our example of a straight, cylindrical bore hole we can deduce two kinds of necessary restrictions to the observable movement. One restriction is object dependent, the other depends on the imaging device.

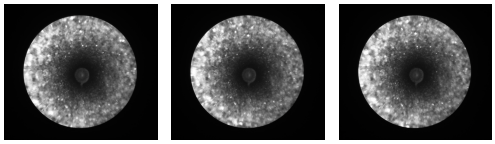

Figure 3: *Three images of sequence taken by flexible endoscope while stepping into bore.*

3.4.1 Object-dependent extensions

Based on the knowledge about the observed object (a straight cylindrical tube), we can introduce restrictions to the region of interest where tracked points are considered as valid. Most endoscopes are designed for a specific minimal working distance. Thus, objects depicted below this distance appear unsharp. Hence, we do not consider image points in areas with a large distance from the optical center.

Secondly, the area around the vanishing point – which is the center of the bore hole and is always close to the optical axis – does not contribute to the intended reconstruction. Additionally, low contrast and tiny details make tracking risky in this area. Therefore, this is the second object-driven subset of tracked points that has to be eliminated.

3.4.2 Device-dependent extensions

To capture image sequences through a commercially available fiberscope, we apply an industrial CCD-Sensor. The camera is connetected via a C-mount adapter to the endoscope's ocular. The image aperture – due to the ocular of the endoscope – is responsible for the circular keyhole that narrows the visible sector. This abrupt change between the circular image and its dark surrounding irritates the applied feature tracker and thus leads to false anchors in connected chains of trails. To eliminate false trail-anchors, the region of interest (ROI) is restricted to inside the aperture circle.

To use a trail for the reconstruction of the corresponding 3-D point, all sections containing point locations outside the specified regions of interest have to be removed. This is done by cutting the trail at its start or its end point. If trails both begin and end outside of the defined ROI, they are removed completely. The bottom sections of figure 4 illustrate the reduced tracked point set.

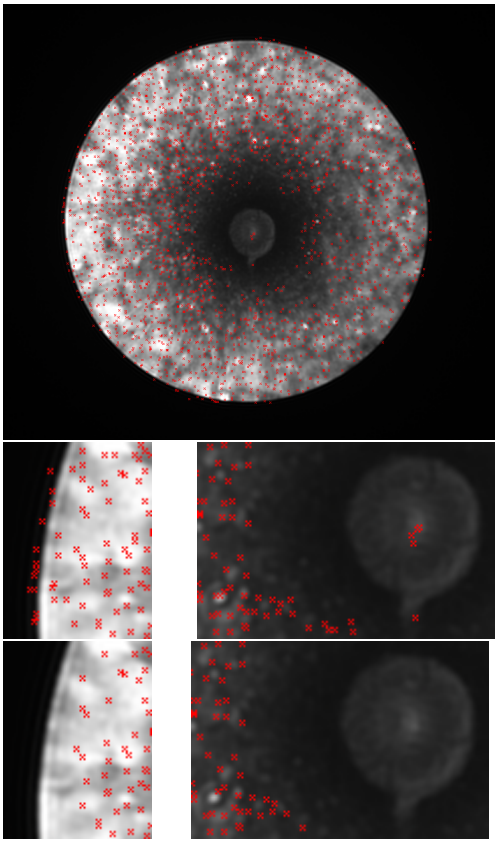

Figure 4: *2nd image from figure 3 with marked tracking points (top). Enlarged sections showing false tracking positions (center) and resulting tracking points after limiting by object-dependent and device-dependent region of interest.*

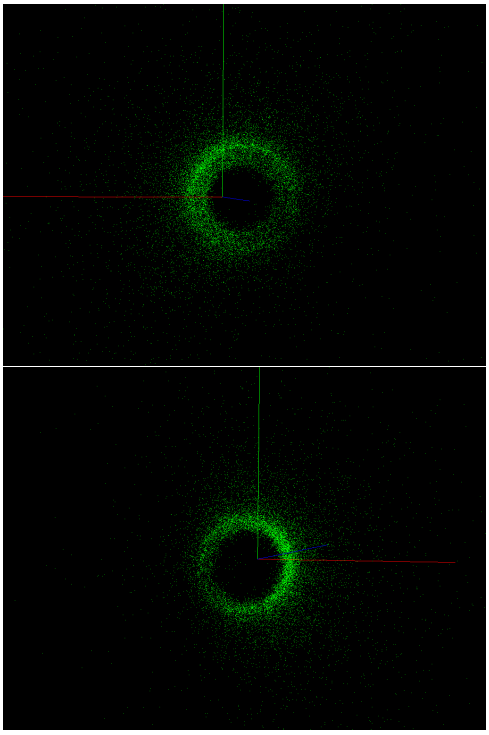

Figure 5: *Profile view of a reconstructed point cloud of cylindric bore hole from unprocessed image data (top). In addition, trails for reconstruction were reduced by cutting them to the region of interest according to section 3.4 (bottom).*

4 Experiments and Results

The extensions to the tracking and reconstruction algorithm – as explained in Section 3.4 – are able to restrict point trails to specific regions of interest. The effects of these object- and device-dependent restrictions are illustrated in Fig. 5. The top point cloud depicts the profile of the reconstructed cylinder, as viewed from the front along the Z-axis. It can be observed as a high blurring around a virtual circle. In the lower point cloud in Fig. 5, the approximately $16,000$ feature points were reduced according to the proposed model- and sensor-dependent restrictions to the region of interest. The factor of eliminated false correspondendes is around 10%. After this correction-step, the points form a more precise circular arrangement.

In section 3.1, an adaptive spectral filtering approach to reduce the honeycomb-structure of fiberscopic images was described. This filtering approach was applied to the fiberscopic image-sequence recorded in the straight, cylindrical bore hole. The effect of applying this specific filter as preprocessing step to fiberscopic image material before localizing and tracking features can be seen in figure 6. The top reconstruction is calculated from points that were localized and tracked in images after our proposed filtering. Compared to the reconstruction from the unfiltered image sequences, as depicted in Fig. 5, the result already shows a more condensed distribution, and less variance of reconstrcuted points. Finally, using the knowledge-driven extensions from section 3.4 and restricting the point set by approximately 10% to the region of interest,

the final reconstruction (see center and lower part of Fig. 6) show the best results.

5 Discussion

Within the scope of our project 'Reconstruction of complex hollow spaces from monocular fiberscopic views' [28], the reconstruction process for such hollows strongly depends on the quality and contents of the input sequence. Since the images are degraded by the fiberoptics of the flexible image conductors, a data driven spectral filtering must be applied before the reconstruction process can take place. If we compare the point cloud calculated from unfiltered image data (Fig. 5 top) with the point cloud calculated from the spectral filtered data (Fig. 6 top), it can be seen that deviation of the points with respect to the ciruclar profile of the boundary of the straight tube has been reduced. The same holds for the knowledge driven post-processing point-elimination step: A comparison of the point cloud calculated from regular image data (Fig. 5 top) with the point cloud calculated from the post-processed data (Figs. 5 and 6 bottom) shows, that the variance of the points with respect to the the boundary of the tube is further decreased. Thus, the proposed filtering and extensions of the 3-D-reconstruction method yield subjectively better results compared to a plain reconstruction scheme. Work in progress currently deals with an objective evaluation scheme of these results by fitting a cylindrical model to the point cloud and calculating the mean and standard deviation of the points with respect to the cylinder model.

Acknowledgements

This work has been funded by the German Research Foundation (DFG) under grant SFB/A7 and SFB/C2.

References

[1] D. B. Board. Stress wave analysis of turbine engine faults. In *Proc's IEEE Aerospace Conference*, volume 6, pages 79–93, 2000.

[2] O. Fujimura, T. Baer, and S. Niimi. A stereo-fiberscope with a magnetic interlens bridge for laryngeal observation. *J.Acoust.Soc.Am.*, 65(2):478–80, Feb. 1979.

[3] H. Haneishi and Y. Miyake. Distortion compensation of electronic endoscope image. *Nuclear Science Symposium and Medical Imaging Conference, 1993.*, 3:1717 – 1721, Nov. 1993.

[4] R. Hartley. Euclidean reconstruction from uncalibrated views. In *Applications of Invariance in Computer Vision*, volume 825 of *Lecture Notes in Computer Science*, pages 237–256. Springer-Verlag, 1993.

[5] H. Hautmann, M. Bauer, K. Pfeifer, and R. Huber. Flexible bronchoscopy: a safe method for metal stent implantation in bronchial disease. *Ann Thorac. Surg.*, 69(2):398–401, 2000.

[6] B. Heigl. *Plenoptic Scene Modeling from Uncalibrated Image Sequences*. ibidem-Verlag Stuttgart, January 2004.

[7] J. Heikkilae and O. Silven. Calibration procedure for short focal length off-the-shelf ccd cameras. *ICPR*, 1996.

[8] F. Inanc. An optical approach to the characterizations of surface flaws induced by fretting. In *Quantitative Nondestructive Evaluation. AIP Conference Proceedings*, volume 615, pages 780–787, 2002.

[9] Intel. Open source computer vision library - reference manual. 2001.

[10] C. Kübler, J. Raszkowski, and H. Wörn. Rekonstruktion eines 3D-Modells aus endoskopischen Bildfolgen. In M. Meiler, D. Saupe, F. Kruggel, H. Handels, and T. Lehmann, editors, *Bildverarbeitung für die Medizin 2002*, pages 201–214, Heidelberg, 2002. 10.-12. März 2002 in Leipzig, Springer Verlag.

[11] K. Martin and C. V. Stewart. Real time tracking of borescope tip pose. In *Proc's 3rd IEEE Workshop on Applications of Computer Vision (WACV)*, pages 123–8, 1996.

[12] A. Meehan. Remote visual inspection equipment for quality control. In *Conference Record WESCON/94 Idea/Microelectronics*, pages 214 – 216, 1994.

[13] A. Müller. *Endoscan: Entwicklung eines Verfahrens zur endoskopischen Vermessung von Trachealstenosen*. Shaker Verlag, Aachen, 2002.

[14] A. Müller, M. Schubert, and E. Beleites. Noncontact three-dimensional laser measuring device for tracheoscopy. *Annals of Otology, Rhinology and Laryngology*, 111(9), 2002.

[15] S. Oshiba, K. Ueno, F. Mochizuki, S. Asaki, and S. Ito. Endoscopical polypectomy of the gastric polyp with electrocoagulation wire loop. *Tohoku J Exp Med.*, 118:Suppl:53–9, 1976.

[16] T. Ozawa, M. Tsuchida, Y. Yamazaki, and T. Arai. Minimally invasive periapical curettage of foreign materials in periapical lesions using a fiberscope. *Int Dent J*, 53(5):314–22, 2003.

[17] C. Poelman and T. Kanade. A paraperspective factorization method for shape and motion recovery. *IEEE Transactions on Pattern Analysis and Machine Intelligence*, 19(3):206–218, mar 1997.

[18] J. Shi and C. Tomasi. Good features to track. In *IEEE Conference on Computer Vision and Pattern Recognition (CVPR)*, pages 593–600, Seattle, Washington, 1994. IEEE Computer Society.

[19] W. Smith, N. Vakil, and S. Maislin. Correction of distortion in endoscope images. *IEEE Transactions on Medical Imaging*, 11:117 – 122, March 1992.

[20] M. Takizawa, M. Tanaka, K. Takami, T. Ohtoshi, K. Ito, M. Satoh, Y. Okada, F. Y. F, and A. Umeda. Increased expression of inflammatory mediators in small-airway epithelium from tobacco smokers. *Am J Physiol Lung Cell Mol Physiol*, 278(5):L906–13, 2000.

[21] T. Thormählen, H. Broscio, and P. N. Meier. Automatische 3D-Rekonstruktion aus endoskopischen Bildfolgen. In M. Meiler, D.Saupe, F. Kruggel, H. Handels, and T. Lehmann, editors, *Bildverarbeitung für die Medizin 2002*, pages 207–210, Heidelberg, 2002. 10.-12. März 2002 in Leipzig, Springer Verlag.

[22] T. Thormählen, H. Broszio, and P. N. Meier. Three-dimensional endoscopy. In *Falk Symposium No. 124, Medical Imaging in Gastroenterology and Hepatology*, Hannover, 2002. Kluwer Academic Publishers.

[23] C. Tomasi and T. Kanade. Detection and tracking of point features. Technical report, Carnegie Mellon University, April 1991.

[24] K. Vijayan Asari, S. Kumar, and D. Radhakrishnan. A new approach for nonlinear distortion correction in endoscopic images based on least squares estimation. *IEEE Transactions on Medical Imaging*, 18(4):345 – 354, April 1999.

[25] F. Vogt, S. Krüger, D. Paulus, H. Niemann, W. Hohenberger, and C. Schick. Endoskopische Lichtfelder mit einem kamerafhrenden Roboter. In T. Wittenberg, P. Hastreiter, U. Hoppe, A. Horsch, H. Handels, and H.-P. Meinzer, editors, *Bildverarbeitung für die Medizin 2003*, pages 418 – 422, Heidelberg, 2003. 9.-11. März 2003 in Erlangen, Springer Verlag.

[26] F. Vogt, S. Krüger, J. Schmidt, D. Paulus, H. Niemann, Werner, and C. Schick. Light fields for minimal invasive surgery using an endoscope positioning robot. *Meth. Inf. Medicine*, 43(4):403 –408, 2004.

[27] C. Winter, S. Rupp, C. Münzenmayer, K. Spinnler, H. Gerhäuser, and T. Wittenberg. Adaptive Rasterreduktion in Aufnahmen von flexiblen Endoskopen durch spektrale Maskierung. In H.-P. Meinzer, H. Handels, A. Horsch, and T. Tolxdorff, editors, *Bildverarbeitung für die Medizin 2005*, pages 45 – 49, Heidelberg, 2005.

[28] C. Winter, K. Spinnler, and T. Wittenberg. 3-D-Akquisition komplexer Hohlräume mit flexiblen Endoskopen. In H. Gerhäuser, editor, *5 Jahre Lehrstuhl für Informationstechnik mit dem Schwerpunkt Kommunikationselektronik*, pages 111 – 120, 2004.

[29] T. Wittenberg, P. Mergell, M. Tigges, and U. Eysholdt. High-speedglottography with a flexible endoscope for the examination of the human larynx during running speech. In T. Lehmann, I. Scholl, and K. Spitzer, editors, *Bildverarbeitung für die Medizin*, pages 119–124, 1996.

[30] K. Yamakawa, T. Kondo, M. Yoshioka, and K. Takakura. Ultrasound guided endoscopic neurosurgery–new surgical instrument and technique. *Acta Neurochir Suppl.*, 61:46–8, 1994.

[31] C. Zhang, J. Helferty, G. McLennan, and W. Higgins. Nonlinear distortion correction in endoscopic video images. *2000 International Conference on Image Processing, 2000.*, 2:439 – 442, Sept. 2000.

[32] Z. Zhang. A flexible new technique for camera calibration. *IEEE Transactions on Pattern Analysis and Machine Intelligence*, 22(11):1330–1334, 2000.

[33] T. Zinßer, C. Gräßl, and H. Niemann. Efficient feature tracking for long video sequences. In *Pattern Recognition, 26th DAGM Symposium*, pages 326–333, Tübingen, Germany, August 2004. Springer-Verlag, Berlin.

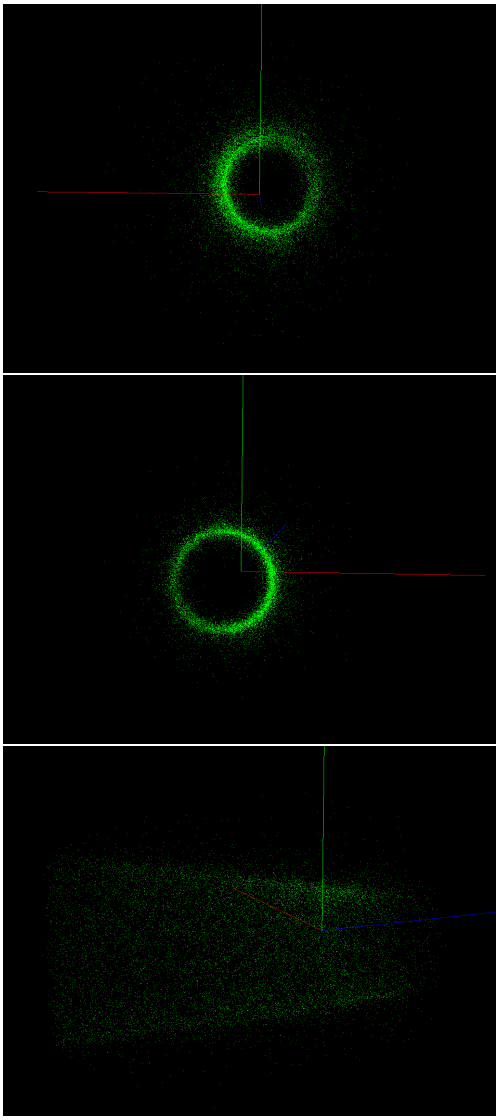

Figure 6: *Profile view of reconstructed point cloud of cylindric bore hole from filtered image data according to section 3.1 (top). In addition, trails for reconstruction were reduced by cutting them to the region of interest according to section 3.4 (center). Bottom: Side view from the reconstructed bore hole*